Progress from ASDEX Upgrade experiments in preparing the physics basis of ITER operation and DEMO scenario development

(article starts on next page)

Progress from ASDEX Upgrade experiments in preparing the physics basis of ITER operation and DEMO scenario development

U. Stroth[1],[*] , D. Aguiam[2], E. Alessi[3], C. Angioni[1], N. Arden[1],
R. Arredondo Parra[1], V. Artigues[1], O. Asunta[4], M. Balden[1],
V. Bandaru[1], A. Banon-Navarro[1], K. Behler[1], A. Bergmann[1], M. Bergmann[1],
J. Bernardo[2], M. Bernert[1], A. Biancalani[1], R. Bielajew[5], R. Bilato[1],
G. Birkenmeier[1],[6], T. Blanken[7], V. Bobkov[1], A. Bock[1], T. Body[1],
T. Bolzonella[8], N. Bonanomi[1], A. Bortolon[9], B. Böswirth[1], C. Bottereau[10],
A. Bottino[1], H. van den Brand[7], M. Brenzke[11], S. Brezinsek[11], D. Brida[1],
F. Brochard[12], C. Bruhn[1], J. Buchanan[13], A. Buhler[1], A. Burckhart[1],
Y. Camenen[14], B. Cannas[15], P. Cano Megias[16], D. Carlton[17], M. Carr[13],
P. Carvalho[2], C. Castaldo[18], M. Cavedon[1], C. Cazzaniga[8], C. Challis[13],
A. Chankin[1], C. Cianfarani[18], F. Clairet[10], S. Coda[19], R. Coelho[2],
J.W. Coenen[11], L. Colas[10], G. Conway[1], S. Costea[20], D. Coster[1],
T. Cote[21], A.J. Creely[5], G. Croci[3], D.J. Cruz Zabala[16], G. Cseh[22],
A. Czarnecka[17], I. Cziegler[23], O. D'Arcangelo[24], A. Dal Molin[25], P. David[1],
C. Day[26], M. de Baar[7], P. de Marné[1], R. Delogu[8], S. Denk[1],[6], P. Denner[11],
A. Di Siena[27], J.J. Dominguez Palacios Durán[16], D. Dunai[10], A. Drenik[1],
M. Dreval[13], R. Drube[1], M. Dunne[1], B.P. Duval[19], R. Dux[1], T. Eich[1],
S. Elgeti[1], A. Encheva[28], K. Engelhardt[1], B. Erdös[22], I. Erofeev[1],
B. Esposito[18], E. Fable[1], M. Faitsch[1], U. Fantz[1], M. Farnik[29], H. Faugel[17],
F. Felici[19], O. Ficker[29], S. Fietz[1], A. Figueredo[2], R. Fischer[1], O. Ford[30],
L. Frassinetti[1], M. Fröschle[1], G. Fuchert[30], J.C. Fuchs[1], H. Fünfgelder[1],
S. Futatani[31], K. Galazka[17], J. Galdon-Quiroga[1], D. Gallart Escolà[31],
A. Gallo[10], Y. Gao[11], S. Garavaglia[3], M. Garcia Muñoz[16], B. Geiger[21],
L. Giannone[1], S. Gibson[32], L. Gil[2], E. Giovannozzi[18], S. Glöggler[1],
M. Gobbin[8], J. Gonzalez Martin[16], T. Goodman[19], G. Gorini[25], T. Görler[1],
D. Gradic[30], G. Granucci[3], A. Gräter[1], H. Greuner[1], M. Griener[1], M. Groth[4],
A. Gude[1], L. Guimarais[2], S. Günter[1], G. Haas[1], A.H. Hakola[33], C. Ham[13],
T. Happel[1], N. den Harder[1], G. Harrer[34], J. Harrison[13], V. Hauer[26],
T. Hayward-Schneider[1], B. Heinemann[1], T. Hellsten[35], S. Henderson[13],
P. Hennequin[36], A. Herrmann[1], E. Heyn[37], F. Hitzler[1], J. Hobirk[1],
K. Höfler[1],[6], J.H. Holm[38], M. Hölzl[1], C. Hopf[1], L. Horvath[23], T. Höschen[1],
A. Houben[11], A. Hubbard[5], A. Huber[11], K. Hunger[1], V. Igochine[1],
M. Iliasova[39], T. Ilkei[22], K. Insulander Björk[40], C. Ionita-Schrittwieser[20],
I. Ivanova-Stanik[17], W. Jacob[1], N. Jaksic[1], F. Janky[1],
A. Jansen van Vuuren[30], A. Jardin[10], F. Jaulmes[29], F. Jenko[1],
T. Jensen[38], E. Joffrin[10], A. Kallenbach[1], S. Kálvin[22], M. Kantor[7],
A. Kappatou[1], O. Kardaun[1], J. Karhunen[4], C.-P. Käsemann[1], S. Kasilov[37],[41],
A. Kendl[22], W. Kernbichler[34], E. Khilkevitch[39], A. Kirk[13], S. Kjer Hansen[1],
V. Klevarova[42], G. Kocsis[22], M. Koleva[1], M. Komm[29], M. Kong[13],
A. Krämer-Flecken[11], K. Krieger[1], A. Krivska[43], O. Kudlacek[1],
T. Kurki-Suonio[4], B. Kurzan[1], B. Labit[19], K. Lackner[1], F. Laggner[9],
A. Lahtinen[4], P.T. Lang[1], P. Lauber[1], N. Leuthold[1], L. Li[11], J. Likonen[1],
O. Linder[1], B. Lipschultz[23], Y. Liu[35], A. Lohs[1], Z. Lu[1],

T. Luda di Cortemiglia[1], N.C. Luhmann[44], T. Lunt[1], A. Lyssoivan[43],
T. Maceina[1], J. Madsen[38], A. Magnanimo[1], H. Maier[1], J. Mailloux[13],
R. Maingi[9], O. Maj[1], E. Maljaars[7], P. Manas[1], A. Mancini[3], A. Manhard[1],
P. Mantica[3], M. Mantsinen[31], P. Manz[1], M. Maraschek[1], C. Marchetto[45],
L. Marrelli[8], P. Martin[8], A. Martitsch[37], F. Matos[1], M. Mayer[1],
M.-L. Mayoral[13], D. Mazon[10], P.J. McCarthy[46], R. McDermott[1], R. Merkel[1],
A. Merle[19], D. Meshcheriakov[1], H. Meyer[13], D. Milanesio[45],
P. Molina Cabrera[5], F. Monaco[1], M. Muraca[1], F. Nabais[2], V. Naulin[38],
R. Nazikian[9], R.D. Nem[38], A. Nemes-Czopf[17], G. Neu[1], R. Neu[1,47],
A.H. Nielsen[38], S.K. Nielsen[38], T. Nishizawa[1], M. Nocente[25],
J.-M. Noterdaeme[1], I. Novikau[1], S. Nowak[3], M. Oberkofler[1],
R. Ochoukov[1], J. Olsen[38], F. Orain[1], F. Palermo[1], O. Pan[1,6], G. Papp[1],
I. Paradela Perez[4], A. Pau[19], G. Pautasso[1], C. Paz-Soldan[35], P. Petersson[48],
P. Piovesan[8], C. Piron[8], U. Plank[1], B. Plaum[49], B. Plöck[1], V. Plyusnin[2],
G. Pokol[43], E. Poli[1], L. Porte[19], T. Pütterich[1], M. Ramisch[49],
J. Rasmussen[38], G. Ratta[50], S. Ratynskaia[48], G. Raupp[1], D. Réfy[22],
M. Reich[1], F. Reimold[30], D. Reiser[11], M. Reisner[1], D. Reiter[11], T. Ribeiro[1],
R. Riedl[1], J. Riesch[1], D. Rittich[1], J.F. Rivero Rodriguez[16], G. Rocchi[18],
P. Rodriguez-Fernandez[5], M. Rodriguez-Ramos[16], V. Rohde[1], G. Ronchi[7],
A. Ross[1], M. Rott[1], M. Rubel[48], D.A. Ryan[13], F. Ryter[1], S. Saarelma[13],
M. Salewski[38], A. Salmi[4], O. Samoylov[1], L. Sanchis Sanchez[16],
J. Santos[2], O. Sauter[19], G. Schall[1], K. Schlüter[1], K. Schmid[1],
O. Schmitz[21], P.A. Schneider[1], R. Schrittwieser[20], M. Schubert[1],
C. Schuster[1,6], T. Schwarz-Selinger[1], J. Schweinzer[1], E. Seliunin[2],
A. Shabbir[42], A. Shalpegin[19], S. Sharapov[13], U. Sheikh[19], A. Shevelev[39],
G. Sias[15], M. Siccinio[17], B. Sieglin[1], A. Sigalov[1], A. Silva[2], C. Silva[2],
D. Silvagni[1], J. Simpson[13], S. Sipilä[33], E. Smigelskis[1], A. Snicker[4],
E. Solano[50], C. Sommariva[19], C. Sozzi[3], G. Spizzo[8], M. Spolaore[8],
A. Stegmeir[1], M. Stejner[38], J. Stober[1], E. Strumberge[1], G. Suarez Lopez[1],
H.-J. Sun[1], W. Suttrop[1], E. Sytova[1], T. Szepesi[22], B. Tál[1], T. Tala[33],
G. Tardini[1], M. Tardocchi[3], D. Terranova[8], M. Teschke[1], E. Thorén[48],
W. Tierens[1], D. Told[1], W. Treutterer[1], G. Trevisan[8], E. Trier[1], M. Tripský[43],
M. Usoltceva[1], M. Valisa[8], M. Valovic[13], M. van Zeeland[35], F. Vannini[1],
B. Vanovac[1], P. Varela[2], S. Varoutis[26], N. Vianello[8], J. Vicente[2],
G. Verdoolaege[42,43], T. Vierle[1], E. Viezzer[1], I. Voitsekhovitch[13],
U. von Toussaint[1], D. Wagner[1], X. Wang[1], M. Weiland[1], A.E. White[5],
M. Willensdorfer[1], B. Wiringer[1], M. Wischmeier[1], R. Wolf[30], E. Wolfrum[1],
Q. Yang[51], Q. Yu[1], R. Zagórski[17], I. Zammuto[1], T. Zehetbauer[1], W. Zhang[51],
W. Zholobenko[1], M. Zilker[1], A. Zito[1], H. Zohm[1], S. Zoletnik[22] and
the EUROfusion MST1 Team[1a]

[1] Max Planck Institute for Plasma Physics, 85748 Garching, Germany
[2] Instituto de Plasmas e Fusão Nuclear, Instituto Superior Técnico, Universidade de Lisboa, 1049-001 Lisboa, Portugal
[3] ENEA, IFP-CNR, Milan, Italy
[4] Department of Applied Physics, Aalto University, Finland
[5] MIT Plasma Science and Fusion Center, Cambridge, MA, United States of America
[6] Physik-Department E28, Technische Universität München, 85748 Garching, Germany
[7] Eindhoven, University of Technology, Eindhoven, Netherlands
[8] Consorzio RFX, Padova, Italy
[9] Princeton Plasma Physics Laboratory, Princeton, NJ, United States of America
[10] CEA/IRFM, Saint Paul Lez Durance, France
[11] Forschungszentrum Jülich, Germany
[12] Institut Jean Lamour, Université de Lorraine, Nancy, France
[13] CCFE, Culham Science Centre, Abingdon, United Kingdom
[14] Aix-Marseille University, CNRS, Marseille, France

15 Department of Electrical and Electronic Engineering, University of Cagliari, Italy
16 Universidad de Sevilla, Sevilla, Spain
17 Institute of Plasma Physics and Laser Microfusion, Warsaw, Poland
18 ENEA, Centro Ricerche Frascati, Italy
19 Ecole Polytechnique Fédérale de Lausanne (EPFL), Swiss Plasma Center (SPC), Lausanne, Switzerland
20 ÖAW, IAP, University of Innsbruck, Innsbruck, Austria
21 University of Wisconsin, Madison, United States of America
22 Wigner Research Centre for Physics, Budapest, Hungary
23 York Plasma Institute, University of York, United Kingdom
24 ENEA Consorzio CREATE, Naples, Italy
25 ENEA, University of Milano-Bicocca, Milano, Italy
26 Karlsruhe Institut für Technology, Karlsruhe, Germany
27 Oden Institute for Computational Engineeringand Sciences, Austin, United States of America
28 ITER Organization, Saint-Paul-lez-Durance, France
29 Institute of Plasma Physics of the CAS, Praha, Czech Republic
30 Max-Planck-Institut für Plasmaphysik, 17491 Greifswald, Germany
31 Supercomputing Center-Centro Nacional de Supercomputación, Barcelona, Spain
32 Department of Physics, Durham University, United Kingdom
33 VTT Technical Research Centre of Finland, VTT, Finland
34 ÖAW, IAP, Vienna University of Technology, Austria
35 General Atomics, San Diego, California, United States of America
36 Laboratoire de Physique des Plasmas, Ecole Polytechnique, Palaiseau, France
37 ÖAW, Graz University of Technology, Graz, Austria
38 Department of Physics, Technical University of Denmark, Kgs. Lyngby, Denmark
39 Ioffe Institute, St. Petersburg, Russia
40 Department of Physics, Chalmers University of Technology, Gothenburg, Sweden
41 Institute of Plasma Physics, National Science Center Kharkov Institute of Physics and Technology, Krakov,   Ukraine
42 Ghent University, Ghent, Belgium
43 ERM/KMS, Brussels, Belgium
44 Electrical and Computer Engineering, University of California, Davis, United States of America
45 ISC-CNR and Politecnico di Torino, Torino, Italy
46 Department of Physics, National University of Ireland, Cork, Ireland
47 Technische Universität München, Garching, Germany
48 KTH Royal Institute of Technology, Stockholm, Sweden
49 IGVP Universität Stuttgart, Germany
50 Laboratorio Nacional de Fusión, CIEMAT, Madrid, Spain
51 Chinese Academy of Sciences, Hefei, China

E-mail: stroth@ipp.mpg.de

CrossMark

Abstract

An overview of recent results obtained at the tokamak ASDEX Upgrade (AUG) is given. A work flow for predictive profile modelling of AUG discharges was established which is able to reproduce experimental H-mode plasma profiles based on engineering parameters only. In the plasma center, theoretical predictions on plasma current redistribution by a dynamo effect were confirmed experimentally. For core transport, the stabilizing effect of fast ion distributions on turbulent transport is shown to be important to explain the core isotope effect and improves the description of hollow low-Z impurity profiles. The L–H power threshold of hydrogen plasmas is not affected by small helium admixtures and it increases continuously from the deuterium to

the hydrogen level when the hydrogen concentration is raised from 0 to 100%. One focus of recent campaigns was the search for a fusion relevant integrated plasma scenario without large edge localised modes (ELMs). Results from six different ELM-free confinement regimes are compared with respect to reactor relevance: ELM suppression by magnetic perturbation coils could be attributed to toroidally asymmetric turbulent fluctuations in the vicinity of the separatrix. Stable improved confinement mode plasma phases with a detached inner divertor were obtained using a feedback control of the plasma β. The enhanced D_α H-mode regime was extended to higher heating power by feedback controlled radiative cooling with argon. The quasi-coherent exhaust regime was developed into an integrated scenario at high heating power and energy confinement, with a detached divertor and without large ELMs. Small ELMs close to the separatrix lead to peeling-ballooning stability and quasi continuous power exhaust. Helium beam density fluctuation measurements confirm that transport close to the separatrix is important to achieve the different ELM-free regimes. Based on separatrix plasma parameters and interchange-drift-Alfvén turbulence, an analytic model was derived that reproduces the experimentally found important operational boundaries of the density limit and between L- and H-mode confinement. Feedback control for the X-point radiator (XPR) position was established as an important element for divertor detachment control. Stable and detached ELM-free phases with H-mode confinement quality were obtained when the XPR was moved 10 cm above the X-point. Investigations of the plasma in the future flexible snow-flake divertor of AUG by means of first SOLPS-ITER simulations with drifts activated predict beneficial detachment properties and the activation of an additional strike point by the drifts.

1. Introduction

ASDEX Upgrade (AUG) is a midsize tokamak with major and minor radii of $R_0 = 1.65$ m and $a = 0.5$ m, respectively. The plasma facing surfaces are covered with tungsten and the magnetic and divertor geometries are like as for ITER. AUG plasmas can match a number of fusion relevant parameters simultaneously, such as high values of the normalized plasma pressure, β_N, the normalized confinement time H_{98}, the Greenwald density fraction $f_{GW} = n/n_{GW}$, and the power density P/R_0. In general, these values can be reached also under detached divertor conditions.

Experiments on AUG are carried out to enhance the physical understanding necessary to better predict the performance of ITER or fusion reactors. Furthermore, new plasma scenarios are explored and control tools developed that can facilitate the operation of a reactor plasma. To achieve these goals, AUG is equipped with a powerful heating system that, with the present power supplies, delivers up to 27 MW of heating power. Neutral beam injection (NBI) of 20 MW power, electron cyclotron resonance heating (ECRH, 6 MW) and ion cyclotron resonance heating (ICRH, 6 MW) are routinely and flexibly combined. In particular, the ECRH system equipped with 8 gyrotrons is very versatile in locally heating the plasma at variable positions [1].

In close contact with ITER and DEMO collaborators, a discharge control system is constantly being further developed and enhanced with real-time capabilities, new real-time sensors and actuators to e.g. avoid disruptions [2] or to control detachment by regulating the vertical position of the X-point radiator (XPR) [3]. The control system is also coupled to a discharge *flight simulator* [4] with a comprehensive plasma model.

The following paper reports on recent results obtained on AUG to challenge the physical models used for predictions, to develop them further where they are still empirical, and to extend them to a wider parameter range and to new discharge regimes. Starting with the integrated modelling effort in section 2, core physics and confinement is treated in section 3, followed by a summary of the investigation of different edge localised mode (ELM)-free regimes in section 4. Section 5 presents results demonstrating the importance of the plasma parameters close to the separatrix for the plasma performance, to finish with results on power exhaust and divertor physics in section 6. The paper closes with a brief summary of the main results.

2. Integrated transport modelling

An important goal of the research effort is to design tools for predicting future reactor discharges based on validated physical models. For this purpose, a workflow for integrated modelling based on engineering parameters (IMEP) was established that is capable of predicting the plasma profiles in stationary phases of AUG H-mode discharges [5, 6]. IMEP is based on the ASTRA transport code, coupled with the HELENA code for high-resolution equilibrium reconstruction

and the MISHKA MHD stability code. With this workflow it is possible to model the kinetic profiles on the entire plasma cross section of AUG discharges when the pedestal conditions are close to the peeling-ballooning stability limit. The separatrix plasma parameters follow from an empirical model with the prescribed gas fuelling and the two-point model for the scrape-off layer (SOL), the pedestal shape is given by peeling-ballooning stability where a critical temperature gradient model is used, and the core plasma profiles from the pedestal top inwards are modeled with TGLF.

Figure 1 shows that the energy content evaluated from fully predictively modeled profiles of stationary H-mode discharges agrees better with the experimental values than estimates derived from the IPB98(y,2) H-mode confinement scaling [5, 7]. The majority of the experimental confinement times have an confinement factor $H_{98} < 1$. This aspect reflects a general property of the plasmas performed on AUG with a tungsten wall [8]. To protect the plasma from impurities, operating with a tungsten wall requires stronger fueling than with a carbon wall. This leads to a relative shift of the density pedestal with respect to the temperature pedestal resulting in a reduced peeling-ballooning limit and thus a weaker pedestal [9]. Furthermore, the increase of confinement with increasing density present in the IPB98(y,2) scaling law is not observed on AUG [8], nor in several other devices with vertically elongated plasmas [10]. In addition, to prevent tungsten accumulation, the discharges are mostly operated with a substantial ECRH power fraction while NBI heating dominates the data represented in the IPB98(y,2) scaling. Therefore, the IPB98(y,2) scaling cannot be fully representative for AUG and revised energy confinement scaling expressions including recent data from metal devices are needed such as the one by Verdoolaege *et al* [10]. However also in AUG, discharges with a confinement factor of $H_{98} > 1$ are obtained particularly in triangular shapes where the edge density can be low. A detailed analysis of the confinement properties of AUG plasmas has been recently published in [8].

With the IMEP software package it is possible to understand the physical reasons for the observed dependencies of profiles and confinement time on engineering parameters including the negative influence of fueling, the positive impact of triangularity, and the positive impact of an increase of plasma current at constant fuelling rate [5]. In parallel to the ASTRA-IMEP workflow, at AUG the first tokamak flight simulator FENIX was developed [4, 11, 12]. FENIX is fully based on the AUG pulse schedule and directly coupled to the AUG control system.

3. Core transport and confinement

Starting with the redistribution of magnetic flux in the plasma center, this section is devoted to results on core heat and particle transport, turbulence studies and the L–H transition power threshold.
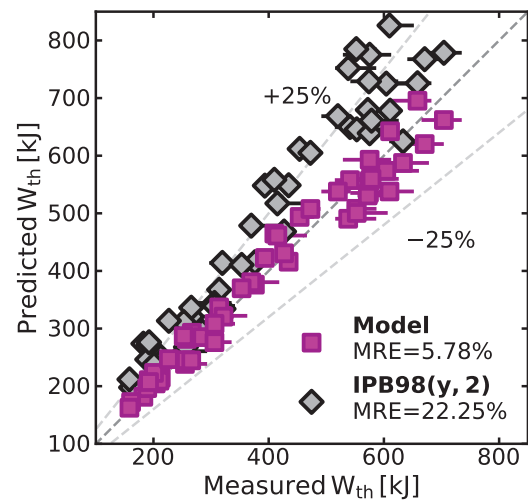
Figure 1. Comparison of the thermal energy content in AUG H-mode plasmas as derived from the IMEP model and from the IPB98(y,2) energy confinement scaling with experimental values. Adapted from [6]. CC BY 4.0.

3.1. Core plasma current diffusion

First an MHD phenomenon is addressed in the plasma center, where elevated central safety factor values of $q_s(0) > 1$ together with sawtooth-free phases were observed, when transport modelling would predict $q_s(0) < 1$ and sawteeth. The experiments were carried out motivated by theoretical results from nonlinear MHD simulations with the MD3D-C code, where it was found that a dynamo driven by a $(1, 1)$ quasi-interchange mode transports poloidal magnetic flux radially outward raising $q_s(0)$ above one [13]. This occurs in a stationary process with continuous redistribution of magnetic flux. In the simulations, this mechanism is activated at high values of the plasma β, when the dynamo drive is sufficiently strong in order to counteract the plasma current diffusion which would lead to a centrally peaked current profile.

Recently, the β threshold for the flux pumping effect was investigated by means of on-axis electron-cyclotron current drive (ECCD) experiments (see figure 2). In a discharge with modest co-ECCD of 100 kA, the sawteeth disappeared when the β value, increased by NBI power steps, surpassed a critical value [14]. A successive increase of the driven current made the sawteeth reappear. Figure 2 also shows that the amount of tolerable co-ECCD without producing sawteeth increases with β [14]. The discharges were analyzed with a combination of the imaging motional Stark effect (IMSE) diagnostic [15] and the IDE equilibrium solver [16, 17]. When sawteeth are suppressed, the IMSE data indicate a flat central q_s profile clamped to values near unity whereas based on neoclassical current diffusion, the equilibrium solver predicts a monotonic q_s profile starting from $q_s(0) < 1$ [14]. The effective charge profile is flat in the plasma centre with values of $Z_{eff} \leqslant 1.5$. Therefore Z_{eff} can only play a minor role for the current profile.

The observed dynamo effect can enable strong ECCD in the center of reactor plasmas, where the current drive efficiency is
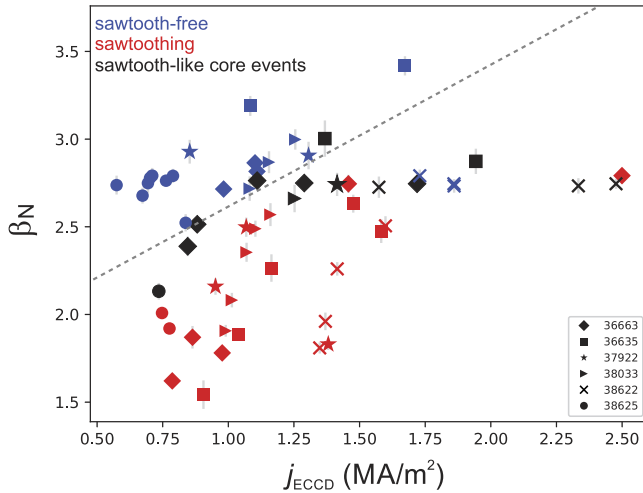
Figure 2. Discharge phases with (*red symbols*) and without (*blue*) sawteeth in the parameter space defined by the normalized plasma β and the volume-averaged non-inductive central current density. Adapted with permission from [14].

high, with flat central q_s profiles as required for enhanced core plasma performance.

3.2. Core heat transport

One of the unresolved issues of core heat transport is the magnitude of the isotope effect and its cause. A novel strategy was used to disentangle the isotope effect in H-mode core and pedestal transport by matching the pedestal profiles with a slight increase of the plasma cross section's triangularity δ for the deuterium case with respect to that in the hydrogen plasmas while keeping heat and particle sources the same [18, 19]. Figure 3 shows the kinetic profiles of a pair of hydrogen and deuterium discharges which both were carried out with a high NBI heating power of about 10 MW and a particle fuelling rate of $7–10 \times 10^{21}$ s^{-1}.

A comparison with modelling results highlights the role of fast ion (FI) populations in reducing turbulent transport in NBI heated discharges. In agreement with results from the theory-based turbulence model TGLF, the core isotope effect was found to be small as long as the fraction of FIs remained below about 30 % of the main ion density [18]. At a higher NBI power with larger fast particle populations, a stronger decrease in ion heat diffusivity was indicated in deuterium with respect to that in hydrogen plasmas leading to substantially higher core ion temperatures, Due to the longer slowing down time of injected deuterium ions compared to that of hydrogen ions, the FI energy content in deuterium plasmas was about 50 % higher.

Nonlinear simulations of these discharges with the gyro-kinetic turbulence code GENE [20, 21] revealed the importance of turbulence stabilization by electromagnetic and FI effects. For both isotopes, the FI distribution from NBI stabilises turbulence and reduces turbulent transport. The stronger effect observed in deuterium plasmas is attributed to the higher content of non-thermal ions [18].

The energy confinement in helium plasmas with dominant electron heating is similar to that in deuterium, while a degradation with an increasing fraction of ion heating is observed. These observations can be theoretically explained by a different role of zonal flows in electron and ion dominated turbulence with different main ions [22].

Low-density L-mode plasmas with dominant electron heating were studied on AUG [23] in particular for their relevance to the first pre-fusion power operation phase of ITER. For this purpose, ECR heated hydrogen and deuterium discharges were performed and modeled with TGLF-SAT1geo, a quasi linear turbulent transport model based on TGLF that includes a turbulence saturation rule and an improvement in the description of geometrical effects [24, 25]. The model reproduced both the central electron temperature and the edge ion heat flux, which is critical for the L–H transition [26, 27], with high confidence. This is seen as a validation of TGLF-SAT1geo also in applications for the prediction of the absorption of X3-mode ECRH in ITER, which critically depends on the central electron temperature.

The same model was also used for the interpretation of cold pulse experiments using impurity laser ablation. The dynamic response of the electron temperature profile following the cooling event in the plasma edge was successfully modeled with the ASTRA transport code with the local transport model TGLF-SAT1. The reason for the—sometimes called nonlocal—fast response of the core temperature was explained by the stabilization of trapped electron modes through an induced and also correctly predicted flattening of the electron density profile [28].

The TGLF model also proved reliable in describing the role of beam ions in reducing ion heat transport in H-mode plasmas. It predicted ion temperature gradient (ITG) turbulence properties observed in experiments, where the ion stiffness was reduced simultaneously with a drop of the electron to ion temperature ratio, T_e/T_i. In addition, a potential role of electron temperature gradient (ETG) driven modes in strongly electron heated H-mode plasmas in limiting the increase of electron temperature gradient was identified by means of linear and nonlinear gyrokinetic simulations with the GKW code [29].

3.3. Core particle transport

The core density profiles of ITER or reactor plasmas will be dominated by transport processes. AUG experiments reproducing reactor conditions of heat, particle and momentum sources and related integrated modelling using ASTRA and TGLF demonstrated the role and dominance of a collisionality dependent turbulent pinch in producing centrally peaked plasma density profiles at reactor relevant low collisionalities [30].

Fast-ion effects turn out to also be important for the description of low-Z impurity transport, which has important consequences for the operation of reactor plasmas. Especially helium transport will determine the amount of fuel dilution in the core of a burning plasma. In order to enhance the physical understanding of low-Z impurity transport, transport studies were carried out for helium and boron. In particular, a new modulation technique was developed and applied
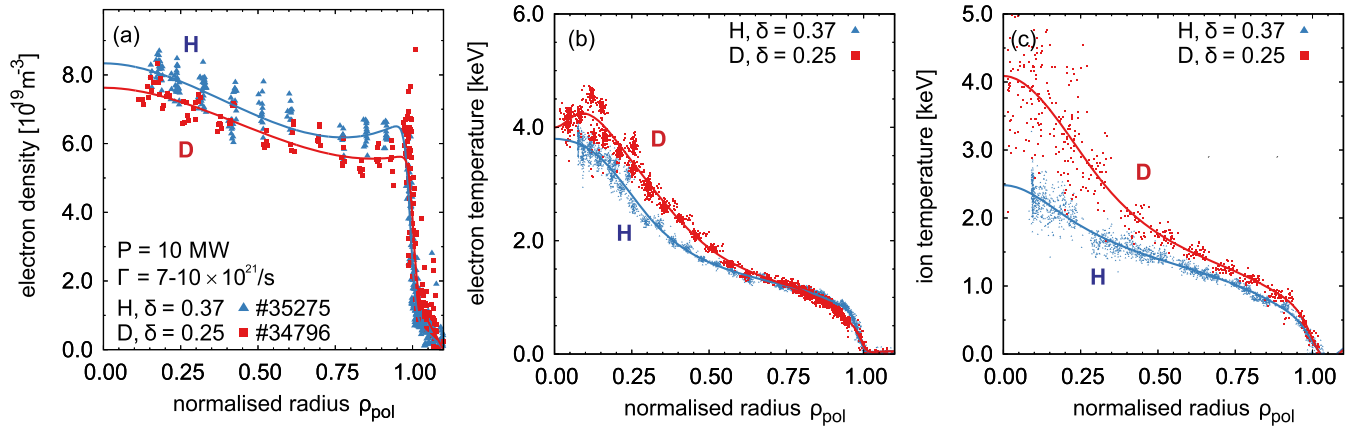
Figure 3. Kinetic profiles of a pair of hydrogen and deuterium H-mode plasmas, where the edge profiles were matched while the source profiles are kept similar. Reproduced courtesy of IAEA. Figure adapted from [18]. © EURATOM 2021.

to boron transport studies to disentangle diffusive and convective transport coefficients [31, 32]. Using this technique, a database of transport coefficients covering a wide range of plasma parameters was assembled and compared to theoretical predictions.

For steep ITGs ($R_0/L_{T_i} > 6$), which coincide with strong NBI heating, outward convection and hollow boron density profiles appear. In contrast, even low levels of electron heating increase both the diffusion and inward convection and result in peaking of the impurity density profiles. Comparisons with a combination of neoclassical and quasi-linear gyrokinetic turbulence simulations (NEO and GKW, respectively) showed good agreement for plasmas with combined NBI and ECR heating.

The hollow boron density profiles, on the other hand, are not fully reproduced by the simulations, particularly around mid-radius. This is demonstrated in the comparison of measured and modeled radial profiles of the boron density scale length in figure 4, where the inclusion of fast ions leads to a clear increase in the outward predicted transport at a normalised radius of $\rho_{tor} = 0.4$. In the modeling, it is a combination of different fast ion effects that leads to the development of hollow boron profiles [33, 35]. The fast ion distribution stabilises ITG driven turbulence and leads to an increase of neoclassical outward convection [35].

However, at mid-radius this effect is insufficient to reach experimental levels due, at least in part, to the relatively small fast ion population at this location. Figure 4 also shows that the results of the simulations are very sensitive to the gradient scale lengths of the background profiles. Small increases in the ion temperature gradient and rotation gradient can change the sign of the predicted convection.

3.4. Core turbulence studies

A validation of the physics models of turbulence codes is also carried out directly on the microscopic level of the fluctuations [36]. For this purpose, measurements of a large set of fluctuation data is assembled on L-mode discharges at two values of the electron temperature gradient length. This implies density fluctuation wavenumber spectra [37], temperature fluctuation
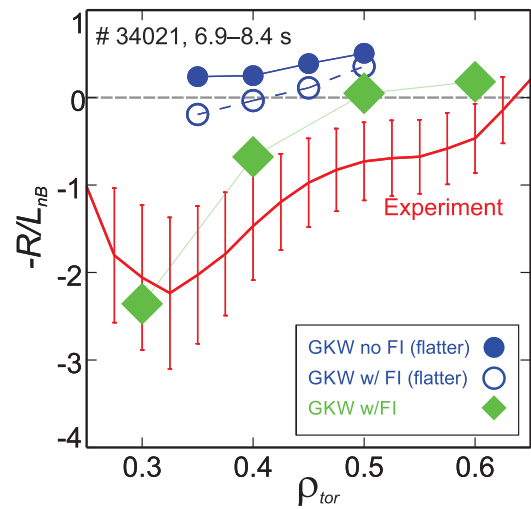
Figure 4. Spectroscopically measured boron density scale length profile from an NBI heated discharge (7.5 MW) compared with modeled profiles form GKW and NEO with and without the fast ion effects included. As a sensitivity test, simulations were also done with *flatter* ion temperature and toroidal rotation velocity profiles (scale lengths were reduced by approx. 10%). Based on results from references [33, 34].

frequency spectra [38], the correlation lengths of both, cross phases between density and temperature fluctuations [38], turbulent flow and phase velocities including zonal flow structures. The experiments are completed and the analysis is ongoing. Comparison of these data with local and global GENE simulations will provide a comprehensive test of the physics models used in the code.

As a first example, the poloidal symmetry of the turbulent propagation velocity was tested using a Doppler reflectometer which probed a radial and poloidal region around the outer midplane. It turned out that the interpretation sensitively depends on the background density profile. From careful analysis, it was concluded, that the flows on the outboard side are poloidally symmetric, where on each flux surface fluctuations propagate with the same velocity at all wavenumbers.
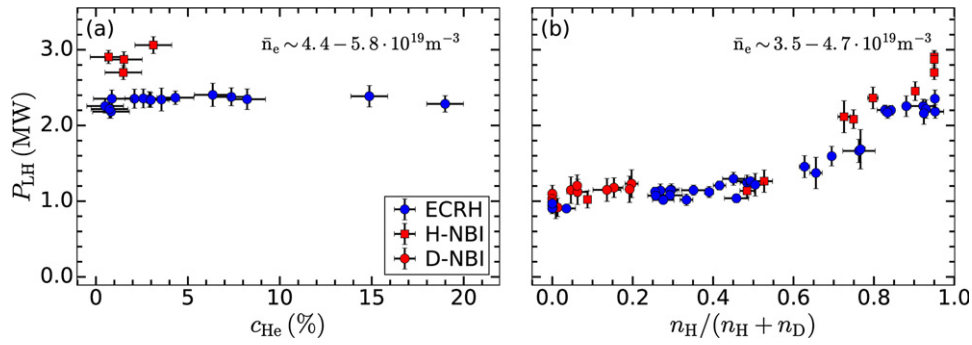
Figure 5. Dependence of the L–H power threshold values in hydrogen discharges as function of the helium content (*a*) and for a transition from a pure deuterium to a hydrogen plasma (*b*). Symbols indicate different heating beams (H or D NBI) and ECRH plasmas. Reproduced courtesy of IAEA. Figure adapted from [41]. © EURATOM 2020.

A comparison with spectroscopic measurements showed that this velocity is close to the $E \times B$ drift velocity [39].

3.5. L–H power threshold

Due to the absence of reliable physical models for the L-mode plasma edge, predictions for the power threshold for L–H confinement transitions, P_{LH}, rely on experimental scaling laws. In particular, the dependence of P_{LH} on the isotopic mass must be known to predict the performance of ITER in the pre-nuclear phase in hydrogen or helium and for the D–T phase. An earlier study on JET indicated a beneficial 40 % reduction of P_{LH} when small concentrations of helium were added to NBI heated hydrogen plasmas. Furthermore P_{LH} increased to the hydrogen level when even a small amount of hydrogen was admixed to deuterium plasmas [40].

Figure 5 shows comparable experiments performed on AUG. The left figure shows that the threshold power did not change and remained at the hydrogen level, when up to 20 % of helium was added to the hydrogen plasmas. The data was obtained from both ECRH and hydrogen NBI heated discharges. For the right figure, a continuous transition from a pure deuterium plasma to a pure hydrogen plasma was performed. The data from the different heating schemes consistently shows a continuous increase of P_{LH} with hydrogen concentration from the D level to the H level. A stronger increase starts only above a relative high hydrogen content of about 60 %. These differences from the JET results need further investigations.

Power balance analyses show that the ion heat flux through the separatrix, which is known to be a key quantity for the L–H transition on AUG [26], is independent of the helium concentration and heating scheme [42]. In hydrogen and deuterium plasmas, the L–H transitions happen at similar values for the neoclassical $E \times B$ shearing rate [27]. Spectroscopic measurements of the edge radial electric field at the L–H transition of hydrogen and deuterium plasmas were also consistent with the observation that the neoclassical $E \times B$ shear, given by the ion pressure gradient, is the key physical parameter for turbulence suppression. The transition in hydrogen and deuterium plasmas is found to occur at the same $E \times B$ velocity [43].

4. Plasma scenarios without large ELMs

Large (type-I) ELMs are considered critical for fusion reactors to the extent that they must be avoided altogether. Therefore, it is important to search for robust small or no ELM regimes, that simultaneously have H-mode-like confinement and can be operated at high density where the divertor can be in a detached state. This section summarizes recent studies of six such regimes. An earlier overview article is reference [44]. It turns out, that the most promising candidates for regimes without large ELMs have in common, that turbulent fluctuations and more or less coherent modes near the separatrix cause transport that changes the pressure gradient of the H-mode pedestal in such a way that the peeling-ballooning limit is not reached and type-I ELMs do not occur.

4.1. ELM suppression by magnetic perturbations

On AUG, the edge density was identified to be the leading parameter for ELM mitigation with magnetic perturbation fields [45]. At low densities the smallest relative pedestal energy losses are observed when a magnetic perturbation field with a toroidal mode number of $n = 2$ is applied, inducing a so-called *density pump-out*.

In recent experiments, the physical origin of the density pump-out was investigated [46]. By toroidal rotating of the $n = 2$ perturbation field, a reflectometer observed toroidally asymmetric broad-band fluctuations with frequencies up to 150 kHz at the outer midplane. The fluctuation spectrum is locally quenched at a certain phase angle of the field perturbation. The fluctuations appear simultaneously with a drop in edge density associated with a density pump-out and are held responsible for it. To identify the transport losses caused by the fluctuations, their dynamics was compared to that observed with a poloidal array of Langmuir probes on the outer divertor target. It was found that the toroidal asymmetry of the turbulence at the outboard midplane maps along the magnetic field lines to the divertor. High and low fluctuation amplitudes at the plasma edge are magnetically connected to high and low particle transport measured in the divertor [46].
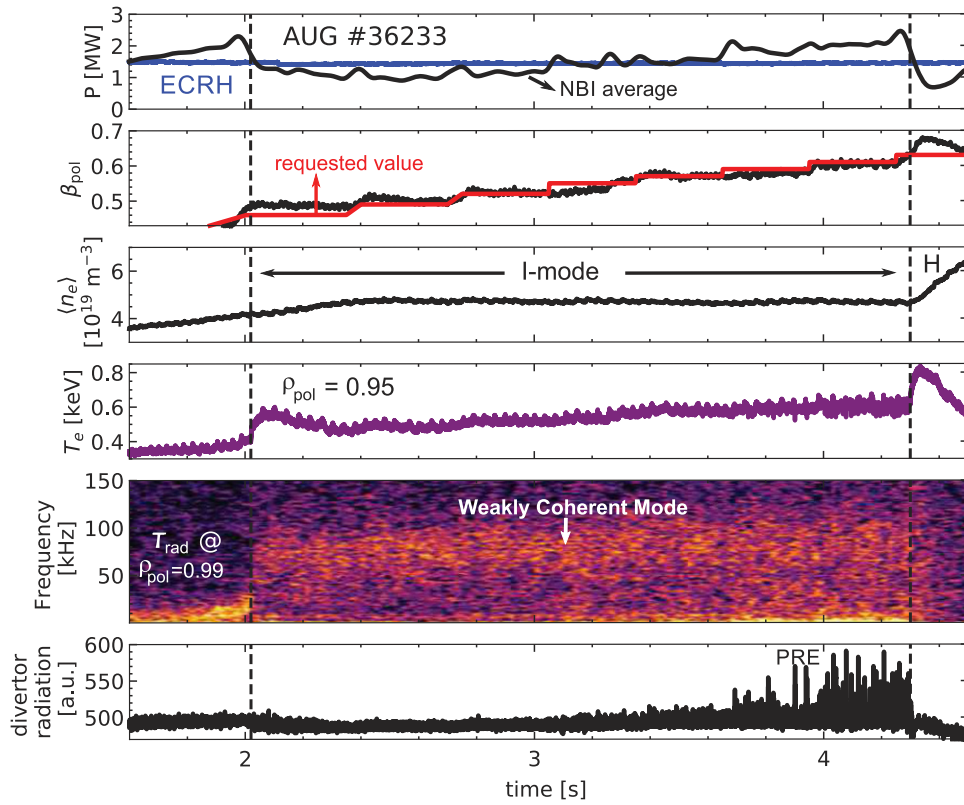
Figure 6. Time traces of I-mode discharge parameters, where the plasma β_{pol} was feedback controlled via the NBI power. The WCM appears in the spectrogram of the ECE radiation measured with a channel close to the separatrix. Close to the I–H transition, pedestal relaxation events (PRE) are visible in the divertor radiation signal. Reproduced courtesy of IAEA. Figure adapted from [53]. © EURATOM 2020.

These observations lead to the interpretation that turbulence near the separatrix causes the density pump-out which reduces the edge pressure gradient and in turn leads to peeling-ballooning stability and ELM suppression. The formation of magnetic islands due to the perturbation field is not indicated on AUG [46].

4.2. Improved confinement mode

The *improved confinement mode* (I-mode), which was observed on several tokamaks [47–50], has a number of attractive properties with respect to a reactor plasma. It can be achieved with pure electron heating and shows neither impurity accumulation nor large ELMs. The I-mode occurs in an unfavorable magnetic configuration, i.e. the ∇B drift points away from the active divertor, resulting in a higher L–H power threshold. On AUG, the I-mode is routinely achieved as long as the heating power remains below the H-mode threshold value [51, 52]. The operating space was also expanded to NBI heating, where stationary I-mode phases were achieved using active β feedback control.

Figure 6 depicts such a discharge, where the required β value was stepwise ramped up by feedback controlled NBI power raising to a total heating power of about 4 MW [53]. After an increase in the edge electron temperature, indicating an electron heat transport barrier, a stationary I-mode phase develops with a weakly coherent mode (WCM) in the range 50–100 kHz. In the particle transport channel, the transport

barrier is not visible and the density remains constant. Intermittent transport events associated with the WCM become more dominant with increased heating power until the I-mode phase ends with a transition to H-mode when values of $\beta_{pol} \approx 0.6$ and $H_{98} \approx 0.9$ were reached. In the phase before the transition, larger edge relaxation events (PREs) are observed. They are smaller than type-I ELMs but can be expected to be detrimental for a reactor divertor and therefore must to be avoided [53].

The operational window for I-mode discharges was investigated on the basis of a database with density and electron temperature pedestal values from plasmas in different confinement regimes. The data from L-mode, I-mode and H-mode plasmas are clearly separated by electron pressure isobars. I-mode pedestal relaxation events occur only where the edge plasma pressure is close to the isobar above which the operational space of H-mode discharges begins [53]. This study highlighted the importance of the edge electron pressure for a stable operation of I-mode discharges and also the challenge of extending the regime to higher heating powers.

Furthermore, nitrogen seeding of I-mode discharges was tested as a way to combine the I-mode regime with a detached divertor [54]. In these experiments, the seeding rate was ramped to a maximum nitrogen core concentration of about 1.5 %. The β window in which the I-mode can exist becomes wider and shifts to higher values. This is not due to increased

radiation, but rather due to increased edge transport as nitrogen is introduced into the plasma. While complete detachment was not obtained, the inner divertor was detached along with a reduction of the heat flux on the outer divertor at a confinement factor of $H_{98} = 0.9$ [54].

A physical picture of the I-mode was derived from simulations using the gyro-fluid code GEMR [55]. Based on the experimentally justified assumption that at the separatrix the ion temperature is higher than the electron temperature and the ion temperature gradient is shallower than that of the electrons, the strong drive of the ITG turbulence is removed. Consequently, the L-mode turbulence turns out to be drift-wave like before the transition. It is shown, that the L–I transition is caused by a suppression of small scale turbulent fluctuations by finite Larmor radius effects and the large scales by phase randomization. The WCM appears as a remnant of the drift wave turbulence spectrum. The simulations reproduce the intermittent transport related to the WCM and also clarify the origin of the I-mode operation window in heating power, magnetic field strength, and collisionality. The fact that a transport barrier forms only in the electron heat channel is attributed to the dissipation of the electron temperature fluctuations by parallel heat conductivity at low collisionalities [55].

4.3. ELM-free H-mode

Recently, stationary ELM-free phases of H-mode discharges were observed on AUG [56]. Closer inspection revealed the similarity of key properties to those of the enhanced D_α H-mode (*EDA H-mode*) from Alcator C-Mod [57–59]. In contrast to the I-mode discussed above, the ion ∇B drift is in the favourable direction and the density pedestal is H-mode like. It has high energy confinement ($H_{98} = 0.9$–1.3) and high density ($f_{GW} = 0.8$–0.9) without impurity accumulation. This makes the EDA H-mode a candidate for a fusion reactor regime. On AUG this ELM-free regime is accessed when the ECRH power is above the L–H threshold P_{LH} and it can be sustained with 50 % of the heating power coming from NBI. Key elements to reach this regime are strong gas puffing and a relatively high safety factor while plasma elongation is favourable to make it more robust [56].

Also on AUG, the EDA regime exhibits the characteristic quasi coherent mode (QCM) with frequencies decreasing from the range 40–80 kHz after the transition to 15–50 kHz during the stationary phase. The mode frequency spectrum broadens under strong gas puffing. The QCM is localized close to the separatrix or in the region of steep pressure gradient and causes transport to the divertor. The toroidal mode number is about $n = 20$ and the mode propagates in the electron diamagnetic direction. This leads to a pedestal pressure profile close to the ballooning but far from the peeling limit [56].

While the regime appears to be compatible with nitrogen seeding for divertor detachment, main challenges in terms of reactor relevance are the limited power window and the high safety factor under which it exists. Without impurity seeding, the EDA regime develops ELMs when the total heating power exceeds about 3 MW. Shaping, gas fuelling and higher current increase the acceptable power before ELMs occur. However,

in recent experiments with argon seeding it was possible to increase the heating power up to about 8 MW [60]. In such discharges, the argon seeding rate was the feedback actuator with the power crossing the separatrix as control variable. The latter was derived from the difference of the total heating power and the real time bolometric measurements of the radiated power from inside the separatrix [61]. Since argon radiates mainly from the plasma edge region, the heat flux through the separatrix could be kept below the threshold value for the transition to an ELMy H-mode [60]. A more robust extension of the power window and the compatibility with lower safety factors remain the challenges to be overcome for this regime.

4.4. Quasi continuous exhaust regime

Some time ago it was observed at AUG that in strongly shaped H-mode plasmas strong gas fuelling can suppress type-I ELMs [62–64]. The large ELMs that cause high transient divertor power loads are replaced by more frequent and smaller edge relaxation events, also known as small, type-II or grassy ELMs, leading to *quasi continuous power exhaust* (QCE). Due to its relevance to a reactor plasma scenario, the now called QCE regime has recently been further studied and developed on AUG [65, 66], TCV [67] and EAST [68]. The small ELM regime reported from JET [69] is distinguished from the QCE regime by its low gas puff and edge density.

Figure 7 illustrates the two key ingredients for obtaining the QCE regime, which are high density (left) and the closeness of the magnetic configuration to double null (right) measured by the distance between primary and secondary separatrix at the outer midplane dR_{XP}. As the density rises in a discharge with a constant magnetic configuration (left figure), the type-I ELMs first become smaller and then vanish when a critical density is reached. In the right figure, type-I ELMs reappear at about 4.3 s, when during a QCE phase the elongation is reduced below a critical value of dR_{XP}. Both elements contribute in an additive manner to the formation of a QCE plasma edge.

As in the other ELM-free scenarios, also in the QCE regime it is indicated that transport caused by fluctuations close to the separatrix relax locally the pressure gradient which stabilizes peeling-ballooning modes and thus the large ELMs. In addition to the small ELMs, fluctuations in a frequency range 20–50 kHz are also visible in the magnetics on AUG and JET [64, 70]. These remaining small edge fluctuations, which can also appear in-between type-I ELMs, could be attributed to high-n ballooning modes [65, 67]. These modes become more unstable due to the increasing connection length between the stable high-field and the unstable low-field side in close to double null configurations. Also a study of type-I ELMs on AUG with the non-linear MHD code JOREK [71] proposes a mechanism for the QCE regime related to resistive peeling ballooning modes which appear at high density near the separatrix and prevent pedestal build-up and type-I ELM crashes [72]. In the QCE regime, enhanced filamentary transport at the plasma edge broadens the SOL power fall-off length by up to a factor of 5 as compared to inter type-I ELM values and a density shoulder [73, 74] forms [75].
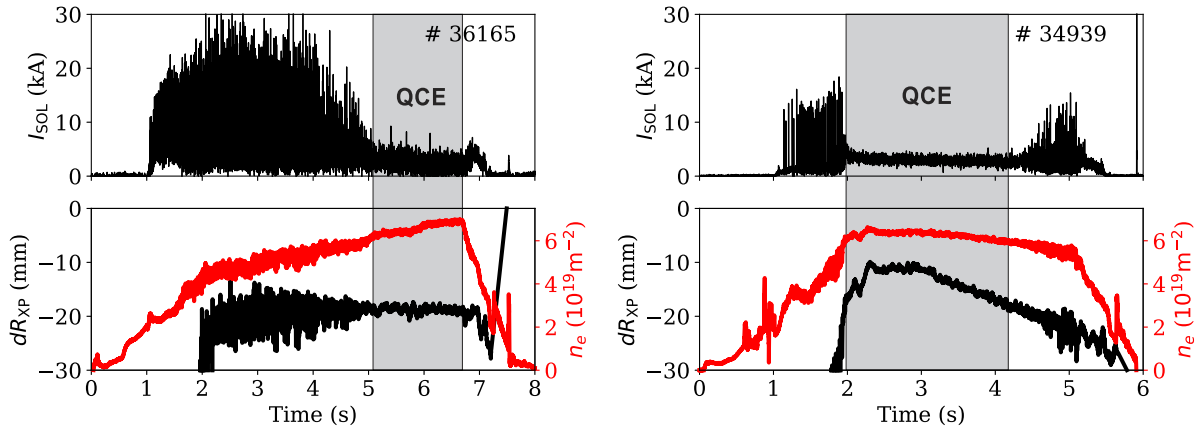
Figure 7. The QCE regime appears when type-I ELMs, detected in the divertor current I_{SOL}, vanish at high density (left) and in configurations close to double null (right), measured by the distance between primary and secondary separatrix at the outer midplane dR_{XP}.

The QCE regime, with separatrix plasma parameters similar to those expected for a reactor plasma, was further developed to integrate high energy confinement and high density with a detached divertor. Furthermore, in order to demonstrate the reactor relevance of the QCE regime, a discharge was designed that did not produce a single type-I ELM [76]. To avoid large ELMs in the early phase of the discharge, it was started with a low plasma current and high safety factor q_{95}, where the ballooning modes near the separatrix are more unstable. After the transition to H-mode, the dynamic increase of the triangularity and moving towards a double-null configuration was accompanied by strong gas fuelling. After reaching a flattop, a double feed-back control was activated: the pre-programmed constant plasma β value was controlled by the NBI heating power and the divertor temperature was reduced by controlled nitrogen seeding in two steps first to 10 eV and later to 5 eV. With a combined ECR, ICR and NBI heating power of 15 MW, this type-I ELM-free demonstration discharge achieved a normalized $\beta_N = 2.1$ and a confinement factor of $H_{98} = 0.9$ with a partially detached divertor. The detachment is accompanied by a modest loss of confinement [76].

This promising regime for ITER and DEMO plasmas will be further developed to achieve lower values of the edge safety factor q_{95} and a robust detachment scenario, where the control via the XPR (see section 6), which also appears during QCE phases, can make an important contribution.

4.5. Further ELM-free scenarios

On AUG, the *quiescent H-mode* (QH-mode), an ELM-free operational regime previously discovered on DIII-D [77], was observed for the first time on a metal wall device [78]. The QH-regime relies on strong plasma rotation and low edge density. In a recent campaign on AUG it was obtained with 8 MW counter-NBI heating. The characteristic modes known from experiments in the carbon-wall AUG, the edge harmonic oscillation (EHO) at 5–10 kHz [79, 80] and the high frequency oscillations at 350–490 kHz [79], were also clearly observed on the tungsten-wall AUG. However, the particle transport driven by the EHO was insufficient to

control the impurity content of the discharges. Consequently, the QH-mode phases remained transient and ended in a radiation collapse. Central ECRH to avoid impurity accumulation resulted in high T_e/T_i ratios, one of the fundamental differences to previously observed QH-modes on the carbon-wall AUG [79]. The stationarity of this regime in a tungsten device and the integration of divertor detachment remain open questions.

First experiments were conducted to investigate the effect of *negative triangular plasma shapes* on the discharge performance of AUG [81]. Shapes with upper and lower triangularity of $\delta_{up} = -0.45$ and $\delta_{lo} = 0.05$, respectively, with an average triangularity of $\delta = -0.2$ were achieved on AUG. In discharges where the ECRH power was stepped up to about 5 MW at 80 % of the Greenwald density, the plasma edge remained in L-mode without ELMs. At the same time the normalized energy confinement was close to $H_{98} = 1$ and also the power degradation followed that known for H-mode confinement [81].

4.6. Summary of ELM-free scenarios

Table 1 summarizes the main characteristics of the small or no-ELM regimes discussed in this section. Although the regimes are obtained through different approaches, transport caused by turbulence or coherent modes at the outer plasma edge was identified as a common mechanism to realize peeling-ballooning stability and type-I ELM suppression.

The goal of an integrated reactor-compatible plasma scenario at high heating power and with a detached divertor is not yet reached in all cases. In particular, it remains a challenging task to integrate high separatrix density and detached divertors into the QH-mode, negative δ plasmas, and the regime with RMP ELM suppression. On the other hand, it is difficult to extend the operation ranges of I-mode and EDA-H-mode plasmas towards high heating powers. At least for EDA H-mode plasmas, dissipating higher power by argon radiation is a promising approach. Currently, the QCE regime, which can combine high confinement with a partially detached divertor, can be operated closest to a reactor relevant integrated scenario.

Table 1. Characteristics of the small or no-ELM regimes (*column* 1) explored on the tungsten wall AUG. For the meaning of the abbreviations refer to the sections listed in *column* 2. The following columns refer to the separatrix density, a key requirement to achieve the regime, the status to combine the regime with a detached divertor and to extend it to high heating power, where *yes* and *no* indicate whether the target has already been reached on AUG or not, respectively. The next columns list the characteristic edge fluctuations and their frequencies and key references from AUG. *Only transient QH-mode phases were achieved.

Regime	Sec.	$n_{e,sep}$	Needs	Detachm.	High P	Edge fluct.	f (kHz)	References
RMP	4.1	Low	$n = 2$ MP	No	Yes	3D	$\leqslant 150$	[45, 82]
I-mode	4.2	Low-mid	Unf. ∇B	Inner div.	No	WCM	50–100	[47, 52]
EDA	4.3	Low-mid	Shaping	Yes	W. Ar seed.	QCM	15–50	[56, 60]
QCE	4.4	High	Shaping	Yes	Yes	Small ELM	0.4–2	[66, 76]
QH-mode*	4.5	Low	Rotation	No	Yes	EHO	2–10	[44]
Neg. δ	4.5	Free	$\delta < 0$	No	Yes	—	Broadb.	[81]

5. Importance of the outer plasma edge

For the ELM-free discharges discussed in the previous chapter, the importance of transport near the separatrix as key element for the stabilisation of peeling-ballooning modes was pointed out. The close connection between fluctuations in the outermost plasma edge and filamentary transport in the SOL is also evident when examining the density fluctuation data in figure 8, which were obtained from a new helium beam diagnostic [83]. The 2D structures of the density fluctuations covering near and far SOL as well as the region up to 1 cm inside the separatrix reflect the weakly coherent and quasi coherent modes of the I-mode and EDA H-mode, respectively, and the relaxation phenomena related to the small ELMs of the QCE regime. Although the characteristic frequencies and degree of intermittency are different, the figures show the close correlation of edge fluctuations with radially outward propagating filaments in the SOL [84].

A close correlation also exists between the electron pressure decay lengths inside and outside the separatrix and the power decay length λ_q over the different confinement regimes L-mode, I-mode and H-mode. This was derived from edge Thomson scattering data on AUG [85]. Furthermore, the scaling behaviour of the power decay length with separatrix plasma parameters was studied beyond the previously addressed range of discharges with low-density attached divertor conditions to high density plasmas reaching the H-mode density limit [86].

The data from the edge Thomson scattering diagnostic combined with the assumption of Spitzer-Härm parallel heat conductivity was used to estimate λ_q. It was found that λ_q, which scales about linearly with the poloidal Larmor radius ρ_{pol} at low densities, undergoes an additional widening at higher collisionalities [86]. This was also seen in BOUT++ transport simulations [87]. A scaling of the form $\lambda_q = 2.1\rho_{pol}(1 + 2.1\alpha_t^{1.7})$ was determined, where increasing values of the normalized collisionality α_t, which is the turbulence parameter introduced by Scott [88] similar to α_d as used by Rogers, Drake and Zeiler [89], describes the transition of the turbulence characteristics from drift-wave to interchange-like, leading to a sharp increase in radial transport around the separatrix. Accordingly, for a value of $\alpha_t = 1$ the power fall-off length broadens by a factor of about 3 also influencing global confinement. H-mode discharges with $\alpha_t > 1$ do not exist on AUG [86].

A subsequent study goes one step further by showing that the separatrix plasma parameters could be responsible for setting important operational boundaries to tokamak plasmas such as the density limit and the L–H transition. Based on a fundamental interchange drift Alfvén turbulence model [88], analytic expressions were derived which, as figure 9 shows, correctly describe the boundaries between the separatrix plasma parameters of L-mode and H-mode discharge intervals as well as the boundary to the density limit [90].

In this model the L-mode density limit (red line) occurs at the transition from electrostatic to electromagnetic resistive ballooning turbulence. The L–H transition (grey line) occurs when the turbulence suppression by the $E \times B$ flow shear caused by the background ion pressure gradient, which is consistent with the neoclassical $E \times B$ shear, is stronger than the turbulent growth rate. Additionally diamagnetic and β stabilization of turbulence are included [90]. As shown in figure 9, L–H transitions (grey line) only occur at separatrix densities $n_{e,sep} \leqslant 2.5 \times 10^{19}$ m^{-3}. In this region, an H–L back-transition will lead to a stable L-mode plasma. At higher densities, L-mode plasmas are disruptive. Here the grey line indicates where a transitions from H-mode to a disruptive L-mode will occur. At high density on AUG, H-mode discharges do not disrupt directly, but undergo an H–L back transition [93] which is partly attributed to the loss of efficiency in the energy transfer from turbulent fluctuations to the shear flow at high collisionality or α_t [90, 94]. The relationship between these observations and the plasma boundary fluctuations, which play a key role in the ELM-free scenarios discussed in section 4, will be addressed in further research.

In figure 9 the ranges of the separatrix plasma parameters for an EDA H-mode and two QCE discharges are overlaid, with the EDA plasma differing from the QCE regime by its lower separatrix density and electron temperature. To discuss the relationship of these data with the boundaries plotted in figure 9, it is important to know that the latter were computed for a fixed magnetic lower single null magnetic configuration. Possible effects due to the proximity to a double null configuration, as used for QCE discharges, on the boundaries are currently not taken into account. Under the assumption that
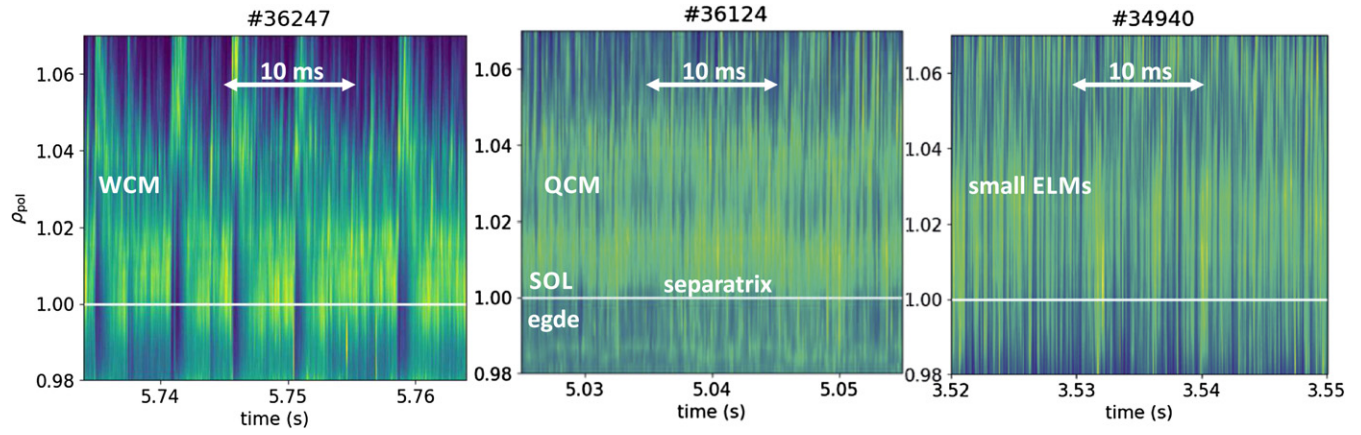
Figure 8. Density fluctuations measured with the helium beam diagnostics across the separatrix during (from left to right) I-mode, EDA H-mode and QCE discharge phases. Adapted from [84], Copyright (2020), with permission from Elsevier. CC BY-NC-ND 4.0.
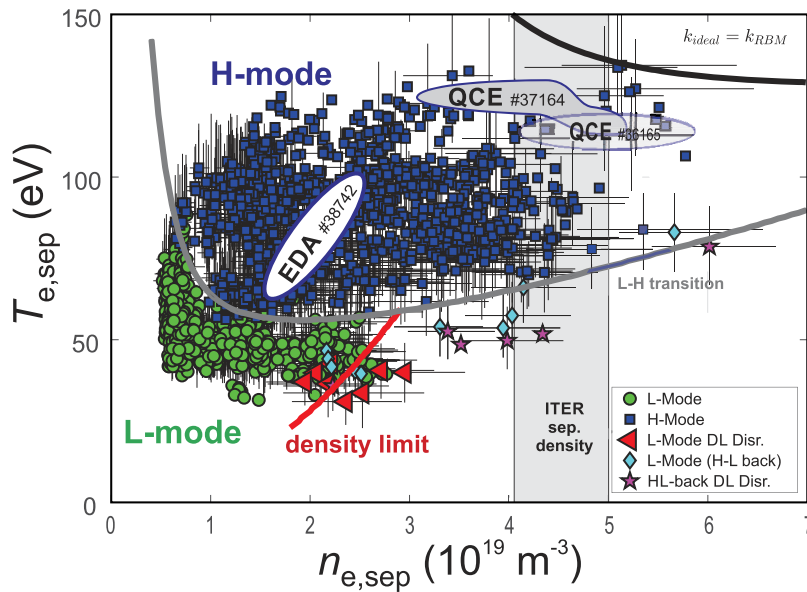

Figure 9. Operational boundaries in the separatrix electron plasma parameter space. The lines applied to circular plasmas; they demark the boundaries for L-mode plasmas to the density limit (red) and an L–H transition (grey). H-mode plasmas can exist below the ideal ballooning limit (black) and above the grey line where a back transition to L-mode occurs which will end in a disruption at densities above 2.5×10^{19} m^{-3}. Symbols mark experimental L- and H-mode data ($\circ$ and $\square$) and disruptive discharges in L-mode ($\triangleleft$). $\diamondsuit$ symbols mark L-mode phases following an H–L back transition prior to the L-mode disruption which is marked as $\star$. The parameter ranges of an EDA H-mode and two QCE discharges are overlayed and the separatrix density range expected for ITER [91, 92] is indicated. Reproduced courtesy of IAEA. Figure adapted from [86]. Copyright (2020) IAEA.

for the near double null configuration the lines for the H–L back transition and the ideal ballooning boundaries limits the parameter range of the QCE discharge towards high densities, the fluctuations observed at the QCE plasma edge could be interpreted as a signature for a loss of turbulence suppression by $E \times B$ shear at high collisionalities or as reaching the ideal ballooning limit, respectively. Exploring this relationship is the subject of ongoing research.

6. Elements of effective power exhaust

On AUG different elements are routinely used for impurity seeding to selectively induce radiative losses in the divertor plasma (nitrogen) [95–97] or the plasma edge (argon and krypton) [60]. Simulations with the impurity transport code STRAHL [98] showed that the radiation efficiencies of the impurities nitrogen and argon in the plasma edge of AUG are strongly enhanced by charge exchange processes between highly ionized impurities and neutral hydrogen [99]. This effect has been neglected so far and when extrapolated to ITER pedestal parameters, it is predicted that it will also significantly increase the pedestal radiation in ITER for the lighter elements neon, argon, and krypton [99]. In this study, the argon densities were evaluated based on improved charge-exchange cross sections which were deduced from recent charge exchange recombination measurements [100].
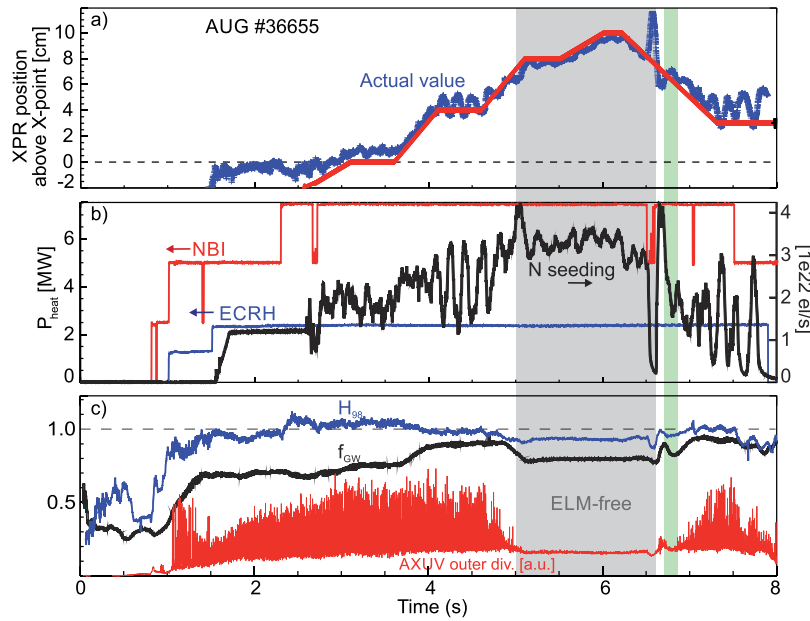
Figure 10. XPR position control (*a*) by nitrogen seeding (*b*) with an ELM-free phase at high confinement and density (*c*). Adapted with permission from [3].

The distribution of seeded nitrogen and argon impurities between inner and outer divertors was studied by means of SOLPS simulations [101]. It was found that a modification of the main particle sources at high seeding rates leads to a reversal of the main ion flows in the SOL, which in turn leads to a redistribution of argon from the outer to the inner divertor. The smaller effect observed with nitrogen seeding is explained by the reduced radiation efficiency and hence smaller effect on the particle source [101]. Furthermore, in the simulations it was found that the divertor impurity retention is determined by the relative positions of the ionization front of the impurities and the impurity stagnation point in the divertor [101]. This relationship was confirmed in a recent multi tokamak study using the SOLPS-ITER code [102].

The X-point radiator refers to a dense, cold and strongly radiating plasma volume located in the confined region above the X-point. It is observed when the outer divertor is detached under nitrogen or argon seeding in the metallic-wall devices AUG [96] and JET [103]. The electron temperature in the XPR volume is of the order of 1–2 eV and the density is well above 10^{20} m^{-3}. This was previously inferred from spectroscopic measurement [96] and recently directly measured with the new divertor Thomson scattering diagnostic. On AUG, the position of the XPR can be derived in realtime from line integrated radiation measurements of an AXUV diode bolometer array and it can be actively manipulated up to 15 cm above the X-point by adjusting the heating power or the impurity seeding rate [3]. Due to the magnetic flux expansion near the X-point, a vertical distance of 10 cm corresponds to a distance from the separatrix at the outer midplane of only a few millimeter.

Figure 10 shows time traces of a discharge, where the X-point radiator position was programmed to be moved 10 cm into and out of the plasma. The measured XPR position follows the preprogrammed waveform with stable discharge phases at all positions. The reduction in seeding rate later in the discharge shows that the process is reversible as the XPR moves back down. For XPR positions higher than 8 cm above the X-point, the type-I ELMs disappear. During the ELM-free phase the radiative power fraction is 90 % and a Greenwald density fraction of $f_{GW} \approx 0.8$ and a confinement factor of $H_{98} = 0.95$ were achieved. Since the occurrence of the XPR is linked to the detachment of the outer divertor [96], this control scheme is a useful tool to control detachment and to avoid the generation of unstable marfes that can lead to disruptions.

To contribute to the investigation of alternative divertor configurations, such as the snowflake divertor [104], a new divertor will be installed on AUG during a one-year shutdown in 2022/2023. While the ITER like lower divertor remains unchanged, the new upper divertor will allow a continuum of configurations between single null and snow-flake [105, 106]. Preparatory SOLPS simulations have indicated that the increased flux expansion in the preferred low-field-side snowflake minus (SF$^-$) configuration should facilitate detachment with nitrogen seeding [107].

Recently, the SOLPS-ITER code [108] was used to investigate the effect of plasma drifts on the SF$^-$ divertor plasma [109]. Compared to a reference case without drifts, the simulation showed an increased asymmetry of the power loads on the inner and outer divertor targets. The $E \times B$ and diamagnetic drifts, which were fully activated in the simulation, increase the power loading on the outer divertor. The drifts also enhance the radial cross field transport and lead to a redistribution of the power between the primary and secondary strike lines of the outer divertor, increasing the power at the strike line connected to the inner SOL. In agreement with experimental observations on TCV [110], the drifts also advect power to a third strike line that is magnetically disconnected from the outer mid-plane SOL [109].

Since the AUG will be equipped with both an ITER-like divertor and a flexible snowflake divertor starting in 2023, the evaluation of the best divertor solution for a fusion reactor will be possible on a single device.

7. Summary

A summary of selected results from recent experiments performed at the AUG tokamak was presented. The aim of the work is to further develop the physical understanding of fusion plasmas and to improve models for reactor plasma predictions as they are integrated in the ASTRA-IMEP code package developed on AUG, which already successfully predicts confinement of AUG H-mode plasmas. The main results are as follows.

In the plasma center, theoretical predictions on magnetic flux pumping were confirmed experimentally. The plasma current redistribution at high β facilitates the operation of advanced plasma scenarios in a reactor with central current drive. For a quantitative modelling of the core heat and particle transport, the effects of fast particle distribution functions on the turbulence play an important role. They are found to be mainly responsible for the core isotope effect, where in deuterium the longer slowing-down time of NBI ions produces a larger fast particle content and thus a stronger reduction of turbulent transport. The inclusion of fast particles also improves the theoretical description of experimentally observed hollow low-Z impurity profiles. On AUG the fast particles originate from NBI or ICR heating. For reactor predictions it will be necessary to transfer this effect to non-thermal α particle distributions.

Important for ITER operation in the pre-nuclear and in the D–T phases is the investigation of the L–H power threshold. It is shown that the threshold power remains on the hydrogen level when up to 20 % of helium is added to a hydrogen plasma and that the threshold power continuously increases from the deuterium to the hydrogen level when the hydrogen concentration is raised from 0 to 100 %.

An integrated naturally ELM-free high confinement plasma scenario would be of great advantage for a safe operation of a fusion reactor. Experimental results from six different confinement regimes without large ELMs were compared on the same tokamak. Transport by turbulence or coherent modes that flatten the pressure gradient of the edge plasma was identified as a common cause of peeling-ballooning stability and ELM suppression. The integration of high edge plasma density and divertor detachment is another obstacle to be overcome on the way to a reactor scenario. This applies in particular to ELM suppression by magnetic perturbation coils, negative δ plasmas and to the QH-mode, while in I-mode plasmas detachment of the inner divertor and reduced power loadings on the outer divertor where achieved by nitrogen seeding. Furthermore, a relevant regime must be developed towards higher heating powers, which remains difficult for I-mode and EDA H-mode plasmas. For the latter, radiative cooling of the plasma edge by argon seeding was demonstrated to be a promising resource.

Plasma shaping and strong gas fuelling appear to be important elements to achieve ELM suppression in the QCE regime, which is the candidate regime that currently operates closest to a reactor relevant integrated scenario. High-n ballooning modes near the separatrix are made responsible for a local flattening of the pressure gradient which enhances peeling-ballooning stability. A QCE demonstration discharge without any large ELM at high heating power and close to the density limit was presented. The discharge combines high confinement with a partially detached divertor. For detachment control of this and other discharges, a feedback controlled X-point radiator is an important element. Such a control scheme was established and used to create stable and detached ELM-free phases at relevant parameters.

The plasma parameters near separatrix, which in AUG are not too far from those in a reactor, prove to be not relevant only for ELM suppression but also for describing important operating limits of tokamak plasmas. Analytic expressions derived from gyro-fluid turbulence equations reproduce the experimentally found boundaries for the L-mode density limit, the L–H transition and the H-mode density limit, which is set by the H–L back transition at high densities. The separatrix parameters of the QCE discharges extend to both high densities and high temperatures inside the H–L transition boundary into the region of expected ITER separatrix parameters.

To evaluate the best divertor solution for a fusion reactor AUG will be equipped with an additional flexible divertor geometry from 2023 on. The first SOLPS-ITER simulations of the expected plasma in a snow-flake minus configuration with fully activated plasma drifts showed favourable detachment properties and an activation of an additional strike point.

Acknowledgments

References

[1] Stober J. *et al* 2015 *EPJ Web Conf.* **87** 02004
[2] Maraschek M. *et al* 2018 *Plasma Phys. Control. Fusion* **60** 014047
[3] Bernert M. *et al* 2021 Control of the X-point radiator in fully-detached ASDEX-Upgrade H-mode plasmas *2020 IAEA Fusion Energy Conf.* (Vienna 2021) (https://conferences.iaea.org/event/214/contributions/) (Virtual: IAEA) EX/7-3
[4] Janky F., Fable E., Treutterer W., Gomez Ortiz I. and Kudlacek O. 2019 *Fusion Eng. Des.* **146** 1926–9 sI:SOFT-30
[5] Luda T., Angioni C., Dunne M.G., Fable E., Kallenbach A., Bonanomi N., Schneider P.A., Siccinio M. and Tardini G. 2020 *Nucl. Fusion* **60** 036023
[6] Luda T. 2021 *PhD Thesis* Aix-Marseille University private comminication
[7] Tardini G. *et al* 2021 Towards fully-predictive transport modelling in ASDEX-Upgrade H-modes *Nucl. Fusion* (private communication)

[8] Ryter F. *et al* 2021 *Nucl. Fusion* **61** 046030

[9] Dunne M.G. *et al* 2017 *Plasma Phys. Control. Fusion* **59** 014017

[10] Verdoolaege G. *et al* 2021 *Nucl. Fusion* **61** 076006

[11] Treutterer W. *et al* 2019 *Fusion Eng. Des.* **146** 1073–6 sI:SOFT-30

[12] Janky F., Fable E., Englberger M. and Treutterer W. 2021 *Fusion Eng. Des.* **163** 112126

[13] Krebs I., Jardin S.C., Günter S., Lackner K., Hoelzl M., Strumberger E. and Ferraro N. 2017 *Phys. Plasmas* **24** 102511

[14] Burckhart A. *et al* 2021 Experimental evidence of magnetic flux pumping at ASDEX-Upgrade *2020 IAEA Fusion Energy Conf.* (Vienna 2021) (Virtual: IAEA) EX/4-1

[15] Ford O.P., Howard J. and Wolf R.C. 2015 *Rev. Sci. Instrum.* **86** 093504

[16] Fischer R. *et al* 2016 *Fusion Sci. Technol.* **69** 526

[17] Fischer R., Bock A., Burckhart A., Ford O.P., Giannone L., Igochine V., Weiland M. and Willensdorfer M. 2019 *Nucl. Fusion* **59** 056010

[18] Schneider P.A. *et al* 2021 *Nucl. Fusion* **61** 036033

[19] Schneider P.A., Hennequin P., Bonanomi N., Dunne M., Conway G.D. and Plank U. 2021 *Plasma Phys. Control. Fusion* **63** 064006

[20] Jenko F., Dorland W., Kotschenreuther M. and Rogers B.N. 2000 *Phys. Plasmas* **7** 1904

[21] Görler T., Lapillonne X., Brunner S., Dannert T., Jenko F., Merz F. and Told D. 2011 *J. Comput. Phys.* **230** 7053

[22] Manas P., Angioni C., Kappatou A., Ryter F. and Schneider P.A. 2018 *Nucl. Fusion* **59** 014002

[23] Kiefer C.K. *et al* 2021 *Nucl. Fusion* **61** 066035

[24] Staebler G.M., Howard N.T., Candy J. and Holland C. 2017 *Nucl. Fusion* **57** 066046

[25] Staebler G.M., Candy J., Belli E.A., Kinsey J.E., Bonanomi N. and Patel B. 2020 *Plasma Phys. Control. Fusion* **63** 015013

[26] Ryter F. *et al* 2016 *Plasma Phys. Control. Fusion* **58** 014007

[27] Cavedon M., Pütterich T., Viezzer E., Birkenmeier G., Happel T., Laggner F.M., Manz P., Ryter F. and Stroth U. 2016 *Nucl. Fusion* **57** 014002

[28] Angioni C., Fable E., Ryter F., Rodriguez-Fernandez P. and Pütterich T. 2019 *Nucl. Fusion* **59** 106007

[29] Ryter F. *et al* 2019 *Nucl. Fusion* **59** 096052

[30] Fable E. *et al* 2019 *Nucl. Fusion* **59** 076042

[31] (a) Bruhn C. *et al* 2018 *Plasma Phys. Control. Fusion* **60** 085011
    (b) Bruhn C. *et al* 2020 *Plasma Phys. Control. Fusion* **62** 049501 corrigendum

[32] McDermott R.M. *et al* 2018 *Plasma Phys. Control. Fusion* **60** 095007

[33] Kappatou A. *et al* 2019 *Nucl. Fusion* **59** 056014

[34] McDermott R.M. *et al* 2019 Validation of low-Z impurity transport theory using charge exchange recombination spectroscopy at ASDEX Upgrade *Proc. EPS Plasma Physics Conf.* (Milano)

[35] Manas P., Kappatou A., Angioni C. and McDermott R.M. 2020 *Nucl. Fusion* **60** 056005

[36] Stroth U. *et al* 2015 *Nucl. Fusion* **55** 083027

[37] Happel T. *et al* 2017 *Plasma Phys. Control. Fusion* **59** 054009

[38] Freethy S.J., Görler T., Creely A.J., Conway G.D., Denk S.S., Happel T., Koenen C., Hennequin P. and White A.E. 2018 *Phys. Plasmas* **25** 055903

[39] Höfler K. *et al* 2021 *Plasma Phys. Control. Fusion* **63** 035020

[40] Litaudon X. *et al* 2017 *Nucl. Fusion* **57** 102001

[41] Plank U. *et al* 2020 *Nucl. Fusion* **60** 074001

[42] Plank U. 2021 *PhD Thesis* LMU Munich to be presented

[43] Cavedon M. *et al* 2020 *Nucl. Fusion* **60** 066026

[44] Viezzer E. 2018 *Nucl. Fusion* **58** 115002

[45] Leuthold N., Suttrop W., Fischer R., Kappatou A., Kirk A., McDermott R.M., Mlynek A., Valovič M. and Willensdorfer M. 2017 *Plasma Phys. Control. Fusion* **59** 055004

[46] Leuthold N. 2020 *PhD Thesis* LMU Munich, Germany

[47] Ryter F. *et al* 1998 *Plasma Phys. Control. Fusion* **40** 725

[48] Whyte D.G. *et al* 2010 *Nucl. Fusion* **50** 105005

[49] Happel T. *et al* 2017 *Plasma Phys. Control. Fusion* **59** 014004

[50] Liu Y.J. *et al* 2020 *Nucl. Fusion* **60** 082003

[51] Ryter F. *et al* 2017 *Nucl. Fusion* **57** 016004

[52] Happel T. *et al* 2019 *Nucl. Mater. Energy* **18** 159

[53] Silvagni D. *et al* 2020 *Nucl. Fusion* **60** 126028

[54] Happel T. *et al* 2021 *Nucl. Fusion* **61** 036026

[55] Manz P., Happel T., Stroth U., Eich T. and Silvagni D. 2020 *Nucl. Fusion* **60** 096011

[56] Gil L. *et al* 2020 *Nucl. Fusion* **60** 054003

[57] Takase Y. *et al* 1997 *Phys. Plasmas* **4** 1647

[58] Greenwald M. *et al* 1999 *Nucl. Fusion* **6** 1943

[59] Mossessian D.A., Snyder P.B., Greenwald M., Hughes J.W., Lin Y., Mazurenko A., Medvedev S., Wilson H.R. and Wolfe S. 2002 *Plasma Phys. Control. Fusion* **44** 423

[60] Kallenbach A. *et al* 2021 *Nucl. Fusion* **61** 016002

[61] David P., Bernert M., Pütterich T., Fuchs C., Glöggler S. and Eich T. 2021 *Nucl. Fusion* **61** 066025

[62] Stober J., Maraschek M., Conway G.D., Gruber O., Herrmann A., Sips A.C.C., Treutterer W., Zohm H. and Team A.U. 2001 *Nucl. Fusion* **41** 1123

[63] Sips A.C.C. *et al* 2002 *Plasma Phys. Control. Fusion* **44** A151

[64] Wolfrum E. *et al* 2011 *Plasma Phys. Control. Fusion* **53** 085026

[65] Harrer G.F. *et al* 2018 *Nucl. Fusion* **58** 112001

[66] Harrer G. 2020 *PhD Thesis* TU Wien, Austria to be published

[67] Labit A. *et al* 2020 *Nucl. Fusion* **59** 086020

[68] Li K. *et al* 2020 *Plasma Phys. Control. Fusion* **62** 095025

[69] de la Luna E. *et al* 2021 Exploring the physics of a high-performance H-mode with small ELMs and zero gas puffing in JET-ILW *2020 IAEA Fusion Energy Conf.* (Vienna 2021) (Nice: IAEA) EX/3-2

[70] Stober J. *et al* 2005 *Nucl. Fusion* **45** 1213

[71] Huysmans G.T.A. 2005 *Plasma Phys. Control. Fusion* **47** 2107

[72] Cathey A. 2021 *PhD Thesis* TUM Munich, Germany

[73] Carralero D. *et al* 2017 *Nucl. Mater. Energy* **12** 1189

[74] Vianello N. *et al* 2019 *Nucl. Fusion* **60** 016001

[75] Faitsch M., Eich T., Harrer G.F., Wolfrum E., Brida D., David P., Griener M. and Stroth U. 2021 *Nucl. Mater. Energy* **26** 100890

[76] Faitsch M. *et al* 2021 High density, high confinement, power exhaust compatible H-mode regime in TCV and ASDEX-Upgrade *Nucl. Fusion* (submitted)

[77] Burrell K.H. *et al* 2001 *Phys. Plasmas* **8** 2153

[78] Viezzer E. *et al* 2019 Development of a QH-mode scenario on ASDEX Upgrade *61st Annual Meeting of the APS Division of Plasma Physics* (Fort Lauderdale, FL)

[79] Suttrop W. *et al* 2003 *Plasma Phys. Control. Fusion* **45** 1399

[80] Suttrop W. *et al* 2004 *Plasma Phys. Control. Fusion* **46** A151

[81] Happel T. *et al* 2020 Experimental investigation of negative triangularity plasmas in the ASDEX Upgrade tokamak *62nd Annual Meeting of the APS Division of Plasma Physics (Virtual)*

[82] Suttrop W. *et al* 2018 *Nucl. Fusion* **58** 096031

[83] Griener M., Wolfrum E., Cavedon M., Dux R., Rohde V., Sochor M., Muñoz Burgos J.M., Schmitz O. and Stroth U. 2018 *Rev. Sci. Instrum.* **89** 10D102

[84] Griener M. *et al* 2020 *Nucl. Mater. Energy* **25** 100854

[85] Silvagni D., Eich T., Faitsch M., Happel T., Sieglin B., David P., Nille D., Gil L. and Stroth U. 2020 *Plasma Phys. Control. Fusion* **62** 045015

[86] Eich T., Manz P., Goldston R.J., Hennequin P., David P., Faitsch M., Kurzan B., Sieglin B. and Wolfrum E. 2020 *Nucl. Fusion* **60** 056016

[87] Li N.M., Xu X.Q., Goldston R.J., Sun J.Z. and Wang D.Z. 2021 *Nucl. Fusion* **61** 026005

[88] Scott B.D. 2005 *Phys. Plasmas* **12** 062314

[89] Rogers B.N., Drake J.F. and Zeiler A. 1998 *Phys. Rev. Lett.* **81** 4396

[90] Eich T. and Manz P. 2021 *Nucl. Fusion* **61** 086017

[91] Kukushkin A.S., Pacher H.D., Pacher G.W., Kotov V., Pitts R.A. and Reiter D. 2013 *J. Nucl. Mater.* **438** S203

[92] Pitts R.A. *et al* 2019 *Nucl. Mater. Energy* **20** 100696

[93] Bernert M. *et al* 2015 *Plasma Phys. Control. Fusion* **57** 014038

[94] Schmid B., Manz P., Ramisch M., Stroth U. *et al* 2017 *Phys. Rev. Lett.* **118** 055001

[95] Kallenbach A. *et al* 2013 *Plasma Phys. Control. Fusion* **55** 124041

[96] Reimold F., Wischmeier M., Bernert M., Potzel S., Kallenbach A., Müller H.W., Sieglin B. and Stroth U. 2015 *Nucl. Fusion* **55** 033004

[97] Bernert M. *et al* 2017 *Nucl. Mater. Energy* **12** 111

[98] Dux R. 2006 STRAHL user manual *Technical Report 10/30 IPP* MPI for Plasma Physics, Garching, Germany,

[99] Dux R., Cavedon M., Kallenbach A., McDermott R.M. and Vogel G. 2020 *Nucl. Fusion* **60** 126039

[100] McDermott R.M., Dux R., Guzman F., Pütterich T., Fischer R. and Kappatou A. 2020 *Nucl. Fusion* **61** 016019

[101] Hitzler F., Wischmeier M., Reimold F. and Coster D.P. 2020 *Plasma Phys. Control. Fusion* **62** 085013

[102] Rozhansky V. *et al* 2021 Multimachine SOLPS-ITER comparison of impurity seeded H-mode radiative divertor regimes with metal walls *2020 IAEA Fusion Energy Conf.* (Vienna 2021) (Nice: IAEA) TH/3-5

[103] Bernert M. *et al* 2017 *J. Nucl. Mater.* **12** 111

[104] Ryutov D.D. and Soukhanovskii V.A. 2015 *Phys. Plasmas* **22** 110901

[105] Lunt T., Zohm H., Herrmann A., Kallenbach A., Dunne M., Feng Y., Neu R. and Wischmeier M. 2017 *Nucl. Mater. Energy* **12** 1037

[106] Lunt T., Pan O., Herrmann A., Teschke M., Dunne M., Feng Y. and Wischmeier M. 2019 *Nucl. Mater. Energy* **19** 107

[107] Pan O., Lunt T., Wischmeier M. and Coster D. 2018 *Plasma Phys. Control. Fusion* **60** 085005

[108] Wiesen S. *et al* 2015 *J. Nucl. Mater.* **463** 480

[109] Pan O., Lunt T., Wischmeier M., Coster D. and Stroth U. 2020 *Plasma Phys. Control. Fusion* **62** 045005

[110] Reimerdes H. *et al* 2013 *Plasma Phys. Control. Fusion* **55** 124027